

OMAE2022-81210

**POWER PRODUCTION FROM A HYDROKINETIC DEVICE:
MASS OF WATER TURBINE**

Azin Lamei

Civil Engineering Department
University of Dundee
Dundee, DD1 4HN, UK

Masoud Hayatdavoodi

Civil Engineering Department
University of Dundee
Dundee, DD1 4HN, UK
Email: mhayatdavoodi@dundee.ac.uk

Stuart Moir

MWNW Consulting
Brathens Eco Business Park
Banchory, AB31 4BW, UK

ABSTRACT

Water current interaction with a hydrokinetic energy converter is studied by use of computational fluid dynamics. Mass of water turbine (MOWT) consists of several thin paddles attached to a conveyor, that are allowed to rotate around the hull. As the incoming current passes under the current energy converter, the paddles move to the direction of the water flow. The motion of the paddles is converted to electricity through the power take-off system of the device. In this study, a two-dimensional computational current tank is generated and the current-structure interaction of a simple geometry is studied. Good agreement between the computed forces and existing data for the same geometry are observed. The velocity and the pressure fields around the MOWT are determined and discussion is provided on the velocity and pressure distribution around the body. Moreover, the forces on individual paddles of the MOWT are computed and compared with the empirical relations. It is found that the current-induced force on the leading paddle is substantially different from that on the downstream paddles due to the change of the flow field. For efficient energy production from this device, optimization is necessary to find a suitable configuration. To obtain an optimum design of the MOWT, the effect of the configuration of the paddles is investigated by considering several combinations and assessing the current-induced loads on the paddles.

Keywords: RANS, Hydrokinetic energy converter, Marine renewable energy, Water turbine, CFD.

Introduction

Renewable energies have received significant attention as a result of increasing desire to move away from fossil fuels in energy production and the increase in energy demand. Although in recent decades a large amount of research has been performed on sustainable energy resources, further developments are necessary to enable large-scale production of low-cost renewable energies. Hydropower is the world's largest and cheapest source of renewable energy, covering approximately 15.9 % of the world's total electricity generation in 2019, see [1]. Hydropower installed capacity reached up to 1330 GW in 2020, with majority in China and Brazil, see e.g. [2] for more information. The hydrokinetic technologies are installed in natural water streams with an optimum velocity, to convert the kinetic energy in the flowing water into electricity, see [3] among others.

Hydrokinetic energy converters are commonly categorized into two main groups, namely (i) turbines and (ii) oscillating devices and rotating paddles, see [4] and [5] among others. Several concepts have been developed within these categories and some hydrokinetic energy converters are built and commissioned in full scales. The turbine hydrokinetic energy converters extract the kinetic energy of the incoming water flow with their rotors. Similar to the wind turbines, the turbines in hydrokinetic energy converters can use both horizontal or vertical axis. For instance, the 1.2-MW Seagen tidal turbine, (see [4]) and Ver-

dant Power 35-kW hydrokinetic energy converter, (see [6]) consist of horizontal axis turbines and the 100 MW Edinburgh vertical axis cross-flow turbine concept [7] is an example of vertical axis turbines. Moreover, they can be fixed on the seabed or mounted on a floating platform. In the latter category, *i.e.* oscillating devices and rotating paddles, the kinetic energy is converted to electricity via the oscillation or the motion of paddles or hydrofoils attached to the device. The Sea Snail tidal energy converter, for instance, consists of several hydrofoils mounted on a frame, see [8]. As the water flow passes the structure, a horizontal force is induced on the hydrofoils, alternatively resulting in their oscillations. The oscillation of the hydrofoils are converted to electricity by use of a generator .

Aquanators are another example of oscillating devices and rotating paddles, see [4] for more details. Similarly, in aquanators a series of hydrofoils or paddles are mounted on a belt sliding on an oval track. The structure is submerged completely or partially underwater. When the tide shifts or the water flow passes the paddles of the device, the belt and consequently the paddles move.

In this study, an aquanator current energy converter, namely the mass of water turbine (MOWT) is introduced. The electricity generated by the MOWT is a function of the paddles' motion and the efficiency of its power take-off system. Here, we focus on the hydrodynamic analysis of the device, and study the hydrodynamic current-induced forces on the paddles. To obtain the forces on the paddles, pressure and velocity fields around the structure need to be determined.

In this study, firstly, the MOWT together with its dimensions are described. The pressure and velocity fields around the MOWT and hydrodynamic forces on its paddles are obtained by use of computational fluid dynamics. The theory, the governing equations, and the applied numerical approach are discussed. A two-dimensional numerical current tank is generated, and the MOWT is added to the numerical current tank. For a given current velocity profile, pressure and velocity fields around the structure are obtained and discussed. The forces on each paddle of the MOWT are computed and compared with empirical relations. The velocity and pressure fields, and the hydrodynamic forces on the paddles are computed for modified configurations of the paddles in order to find an optimum performance and power output of the MOWT. Finally, concluding remarks about the presented analysis are provided.

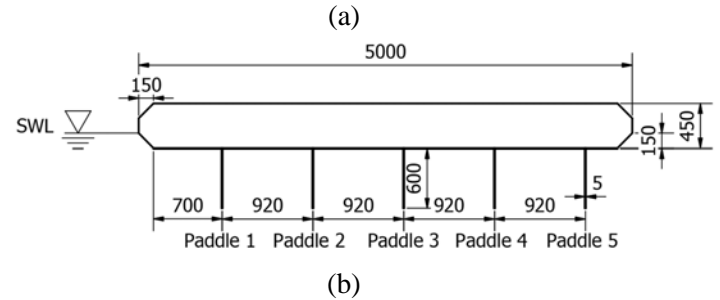
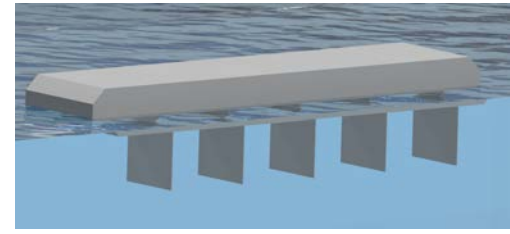


FIGURE 1. (a) A rendered view of the MOWT floating on the water surface, and (b) schematic of the MOWT, showing the geometry and the exact dimensions (in mm) used in this study.

The Mass of water turbine

Mass of Water Turbine (MOWT) is the concept of a hydrokinetic energy converter proposed by Ecosse IP (EIP), [9], and now under development by MWNW Consulting Limited. MOWT aims to convert current energy to electricity and consists of a floating body and a series of paddles and it is kept in place by the use of mooring lines. The paddles are attached to a conveyer and are allowed to move and rotate around the floating body due to the current loads. The motion of the paddles is then converted to electricity by use of a power take-off system. MOWT has been proposed as an energy production solution for slower moving water bodies such as rivers, estuaries and ocean currents where energy is harnessed from the sheer mass of water more so than the speed. The concept is mainly applicable to locations where there is uniform fluid flows (as opposed to oscillatory). The system can operate either floating or fully submerged, e.g. on water surface of a river, or on the seabed in an ocean current.

There are two fundamental questions about this concept, namely (i) how does the fluid interact with the structure, and (ii) what changes to the concept should be made to optimize the efficiency of the system in generating electricity. This study aims to provide insight about these questions.

The theory and numerical solution

An earth-fixed Cartesian coordinate system is chosen with the origin on the still water level (SWL), and y-axis

pointing upwards. The x -axis is parallel to the incoming current direction and z -axis is to the page.

For high Reynolds numbers, the turbulence is important and thus a turbulence model or closure would need to be used to model the flow. Reynolds-Averaged Navier-Stokes (RANS) equations provide a reasonable estimation for this purpose, see [10]. For a homogeneous, Newtonian and incompressible fluid, the RANS equations are given by the following conservation of mass and momentum equations,

$$\bar{u}_{i,i} = 0, \quad i = 1, 2, 3 \quad (1)$$

$$\bar{u}_{j,t} + (\bar{u}_i \bar{u}_j + \overline{u'_i u'_j})_{,i} = g_j - \frac{1}{\rho} \bar{p}_{,j} + \nu \bar{u}_{j,ii}, \quad i, j = 1, 2, 3 \quad (2)$$

where $\bar{f}(x_1, x_2, x_3, t)$ is the time-averaged value of the fluctuating variable, $\vec{u} = u_i \vec{e}_i$ is the velocity vector, and \vec{e}_i is the unit normal vector in the i direction.

There are two commonly used turbulence models for the RANS equations, namely, the $k - \omega$ model and the $k - \varepsilon$ model. Ferziger et al. (2012) [11], have discussed that dissipation is required in equilibrium turbulent flows, *i.e.* whose rates of producing and destruction are in near balance. For the energy equation, the relation between the dissipation, ε , and the turbulent kinetic energy, k , and length scale, L , is written as

$$\varepsilon \approx \frac{k^{\frac{3}{2}}}{L}. \quad (3)$$

Substituting ε into the momentum equation, Eq. (1) gives

$$(\rho \varepsilon)_{,t} + (\rho u_j \varepsilon)_{,x_j} = C_{\varepsilon 1} P_k \varepsilon_{,k} - \rho C_{\varepsilon 2} \varepsilon^2_{,k} + (\mu_{t, \sigma_\varepsilon} \varepsilon_{,x_j})_{,x_j}, \quad (4)$$

where the eddy viscosity $\mu_t = \rho C_\mu \sqrt{k} L = \rho C_\mu \frac{k^2}{\varepsilon}$, and the five parameters usually are given as: $C_\mu = 0.09$, $C_{\varepsilon 1} = 1.44$, $C_{\varepsilon 2} = 1.92$, $\sigma_k = 1.0$ and $\sigma_\varepsilon = 1.3$, see [11]. The model based on Eqs. (3) and (4) is called $k - \varepsilon$ model. The results presented here are obtained by use of the $k - \varepsilon$ model.

The governing equations for both air and water regions of the domain are solved with respect to a scalar function, α , representing the phase of the fluid in each cell, *i.e.* 0 is air and 1 is water. The governing equations are solved in

time domain and the calculation proceeds in time once the velocity of the fluid at each cell is computed.

Domain discretisation: The domain is discretised with finite volume (FV) method and the finite regions in the domain are called control volumes (CV). The conservation equations, Eq. (1) and (2) are applied to each CV and the variable values at the CV surfaces are expressed by interpolation of the ones at the centroid of the CV.

Boundary conditions: Boundary conditions are imposed to all the surfaces in the numerical tank, including the structure. A no-slip boundary condition is imposed on the seabed and the body. The total pressure above the free surface in the air section is equal to atmospheric pressure. Moreover, outlet zones are modelled at the end of the tank to absorb the generated flow in the domain and prevent any reflection back to the computational zone.

The solution algorithm: The four governing equations, RANS equations in x -, y - and z -direction and the continuity equation, Eqs.(1) and (2), introduce four unknowns, the velocity vector components and the pressure. Equations (1) and (2) are solved with pressure-momentum coupling algorithms, namely the semi-implicit method for pressure-linked equations (SIMPLE) for steady-state analysis, the pressure implicit splitting of operator (PISO) for unsteady calculations, and the merged PISO-SIMPLE (PIMPLE) algorithms. In PIMPLE, the SIMPLE algorithm is applied to iteratively compute the pressure in RANS equations, (2) and the results are revised with PISO algorithm, see [11] for more details. In the current study the simulations are conducted with the PIMPLE algorithm. The computations are carried out by use of an open source solver, OpenFOAM, [12] and the boundary conditions for the water and air parts of the domain, seabed, inlet and outlet zones are applied with another open-source library in OpenFOAM, namely *waves2foam*, see [13].

The governing equations are solved for a numerical tank which consists of inlet and outlet, and computational zones, see Fig. 2. The incoming flow is generated at the inlet zone and travels to the computational zone. The test cases are placed within the computational zone, where for instance free surface elevation, hydrodynamic pressure and velocity distribution around the object are computed and reported.

The numerical current tank

A two-dimensional numerical current tank is generated to study the pressure and velocity distribution around the structure and its paddles, see Fig. 2. The numerical tank is 26 m long and the water depth is 5 m. The top surface of

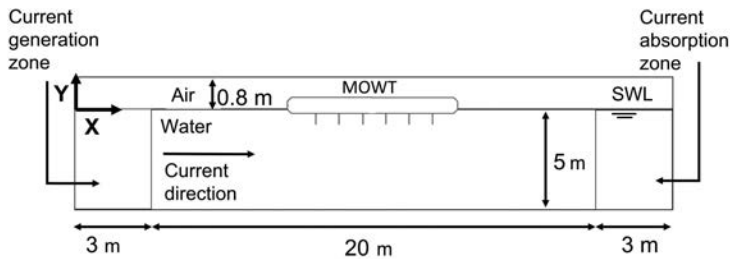


FIGURE 2. Schematic of the computational current tank.

the tank is raised for 0.8 m above the SWL to include the air region. The current generation and absorption zones are 3 m long each. The incoming current profile is uniform from the seabed to the SWL and fixed at 2 m/s. The structure is fixed at the SWL where the draft of the main hull is 0.15 m. A schematic of the computational current tank with the MOWT is presented in Fig. 2.

In the numerical current tank, the current velocity profile is generated at the inlet zone with a ramp function over time. The velocity profile of arbitrary shape develops gradually and enters the domain.

For the given dimensions of the tank, mesh convergence study is conducted in the absence of current and for wave interaction with a fixed box at the SWL, for which laboratory measurements are available for comparison, see [14]. In this study, the wave-induced particle velocities are comparable with our objective current velocity in the numerical current tank, allowing us to perform this analysis for the mesh convergence study. Coarse, medium and fine meshes are generated with respect to the incoming wave height and wavelength. The forces and overturning moment on the box agree well with the analytical solution with medium and fine meshes. Hence, the computations for the current interaction with the MOWT are carried out with the medium mesh. In the absence of the MOWT, the numerical tank is discretized with 260 and 500 elements along its length and depth, respectively. Initially, with the specified mesh, a uniform current profile at 2 m/s is generated in the computational tank for 10 s. The fluid velocity at the middle of the tank is recorded and compared with its objective value along the depth of the tank at $t = 1$ s and $t = 5$ s. Shown in Fig. 3, the computed velocity shows an excellent agreement with the objective current velocity profile. Next, the structure is added to the computational zone with *snappyHexMesh* utility in OpenFOAM. When the MOWT is added to the domain, the mesh around the body is refined. The mesh approximately conforms to the surface by iteratively refining an initial mesh in the domain, where the

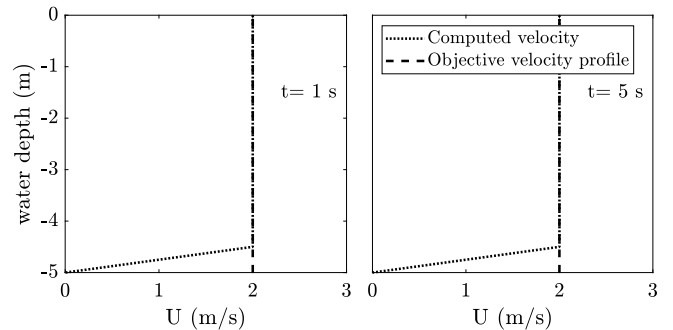


FIGURE 3. Comparison of computed velocity profile and the objective velocity profile over the depth of the tank at $t = 1$ and $t = 5$.

finest mesh is across the surface of the body, see [12]. The mesh refinement allows us to model the flow at the vicinity of the structure more accurately.

Results & Discussion

In this section, firstly, the current-structure interaction study in the numerical tank is assessed. The current-induced hydrodynamic force on a square cylinder is computed and compared with empirical drag force. Next, the MOWT is added to the numerical tank and the velocity and pressure fields around the structure are shown. The forces on the MOWT and the individual paddles are presented. The computations were performed in parallel, using 8 cores, on an Intel W3690 @ 3.47 GHz with 20 GB of memory.

Note that in all cases studied here, the plates (paddles of the MOWT) are fixed and rigid, i.e. there is no deformation or drift of the body or the plates. See e.g. [15–17] for hydroelastic deformation and drift of plates, whether floating at the water surface or submerged.

The current-induced force on a square cylinder

To assess the numerical current tank, the current-induced force on a simple geometry is computed and compared with empirical drag force. In this study, a submerged square cylinder with $L = 150$ mm long (parallel to the flow direction), $W = 1000$ mm wide (to the page), and $D = 150$ mm deep (perpendicular to the flow direction) is located at the middle of the numerical tank, see Fig. 2 and 0.47 m under the SWL. The incoming current velocity is uniform at 0.35 m/s. The empirical drag force on the object is computed as,

$$F_D = \frac{1}{2} C_D A \rho u^2, \quad (5)$$

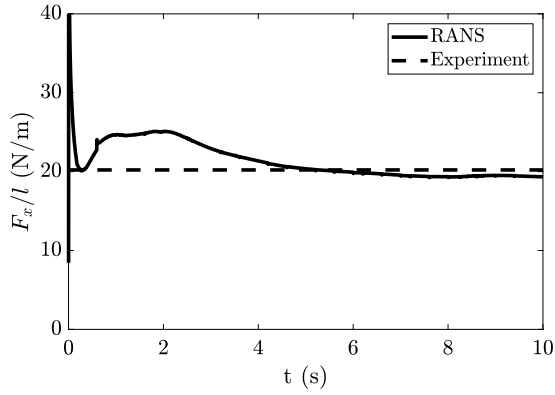


FIGURE 4. Comparison of the two-dimensional horizontal force on the square cylinder and the laboratory measurements of Venugopal et al. (2009), [18].

where C_D is the drag coefficient, ρ the fluid density, u is the fluid velocity and A is the paddle cross sectional area. Venugopal et al. [18] have measured and reported the drag coefficients of the rectangular cylinders for $10^4 < Re < 10^5$ and various aspect ratios, L/D . The drag coefficient for the square cylinder with Reynolds number 5.8989×10^4 and aspect ratio of 1 is 2.18. Figure 4 shows the comparison between the empirical drag force computed by Eq. (5) and the two-dimensional current-induced hydrodynamic force on the cylinder, obtained in the numerical current tank. Shown in Fig. 4, the computed force initially is larger than the drag force at $t < 4$ s, however, it gradually converges to the empirical drag force calculated by Eq. (5). Very good agreement is observed between the computed force and the empirical drag force at $t > 4$ s.

The MOWT

In this section, snapshots of the velocity and pressure fields around the MOWT together with time series of the current-induced forces on the paddles of the device are presented and the results are discussed. The current velocity profile is uniform and constant at 2 m/s from the seabed to the SWL. The simulations are run for 15 s with 175130 cells in the domain and took approximately 2 days and 1 hour.

The velocity and pressure field around the MOWT

The velocity field around the structure is presented in Fig. 5 at $t = 0.6$ s, 1.2 s, 3 s and 5 s. The length and the direction of the vectors represent the magnitude and the direction of the flow velocity, respectively. Shown in the four snapshots, the fluid velocity downstream the main hull and in the gaps between the last four paddles decrease to ap-

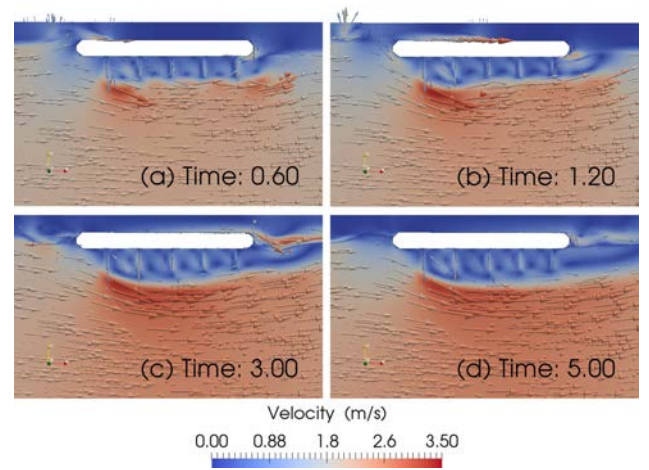


FIGURE 5. Snapshots of the velocity field around the MOWT at (a) $t = 0.6$ s, (b) $t = 1.2$ s, (c) $t = 3$ s and (d) $t = 5$ s.

proximately zero. However, below the paddles, the velocity increases to values slightly more than the current velocity. As time proceeds, vorticities between the paddles and downstream the MOWT are formed. Little to no change are observed at $t > 5$ s. Observed in Fig. 5, the body creates a wake region in which the velocity (and pressure as shown later) is significantly impacted.

Next, we take a closer look into the velocity profiles upstream and downstream of the paddles. For this purpose, velocity is recorded along the vertical lines, 10 cm upstream and downstream of the paddles. The computed velocity is shown from 20 cm below the paddles up to the top of the paddles, where they are connected to the hull. The computed velocities for paddles 1 and 3, for instance, are presented at $t = 0.6$ s and 8 s, in Fig. 6, and are compared with the incoming current velocity profile. In general, the computed velocity profiles undergo small changes over time, however they are significantly smaller than the incoming current velocity profile both upstream and downstream the paddles. The spatial average of the difference between the upstream and downstream velocities for paddles 1 and 3 with respect to the incoming current velocity is approximately 100.5% for 10 s simulation time.

The pressure field around the structure is shown in Fig. 7 at at $t = 0.6$ s, 1.2 s, 3 s and 5 s. The hydrodynamic pressure increases significantly at the front of the main hull at $t = 0.6$ s. Moreover, high and low pressure distributions at the upstream and downstream of paddle 1, respectively, are observed. However, the rest of the paddles experience low hydrodynamic pressures in both their upstream and downstream sides at $t = 0.6$ s. At higher times, the high pressure upstream the main hull and upstream paddle 1 de-

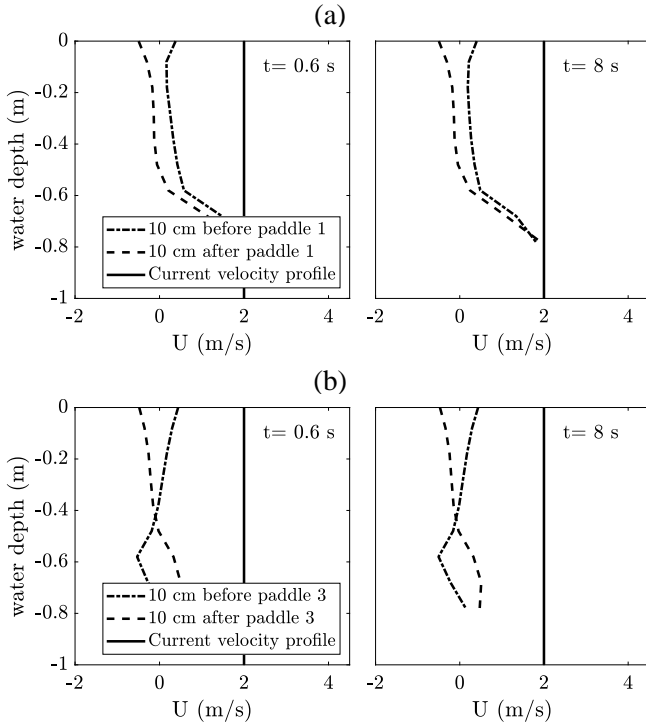


FIGURE 6. Velocity profile along the paddles at 10 cm upstream and downstream of (a) paddle 1 and (b) paddle 3 at $t = 0.6$ and $t = 8$.

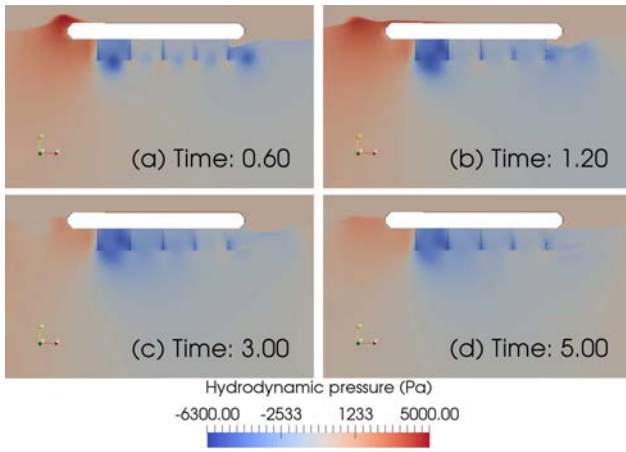


FIGURE 7. Snapshots of the pressure field around the MOWT at (a) $t = 0.6$ s, (b) $t = 1.2$ s, (c) $t = 3$ s and (d) $t = 5$ s.

crease slowly. Similarly, the pressure between paddles 1 and 2 drops to the minimum pressure in the domain. Furthermore, the pressure distribution for paddles 3, 4 and 5 does not change significantly over the simulation time.

Time series of the normalised total pressure at three depths along the paddles on their upstream and downstream surfaces are presented in Fig. 8, for paddles 1, 2, 3, 4 and 5. The pressure in these figures are normalised by the com-

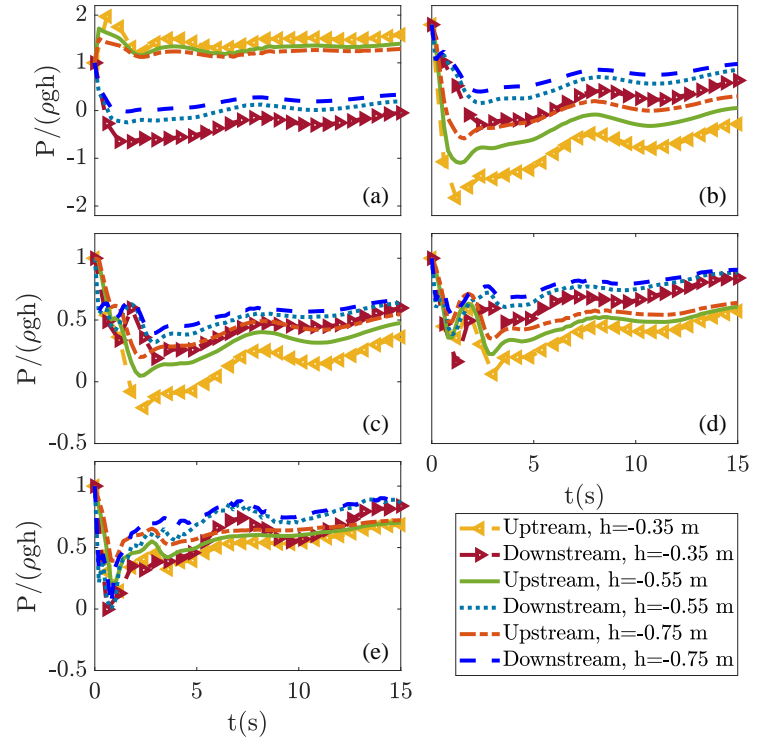


FIGURE 8. Normalized total pressure at three points along (a) paddle 1, (b) paddle 2, (c) paddle 3, (d) paddle 4 and (e) paddle 5 at both upstream and downstream.

puted hydrostatic pressure (ρgh) at the depth h of the considered points on the paddles. The pressure upstream paddle 1 is significantly larger than the pressure on its downstream, which is observed in the snapshots shown in Figs. 7 for the presented simulation times. Moreover, paddles 2 to 5 experience a significant drop at their upstream pressure for $t < 2$ s.

As shown in Figs. 5 and 7, each paddle experiences different hydrodynamic velocity and pressure at its upstream and downstream, and hence their current-induced forces are not comparable with each other. Two-dimensional hydrodynamic forces on individual paddles are obtained by integrating the hydrodynamic pressure on the paddles. Since the simulations are conducted for a two-dimensional numerical tank, the forces on the paddles are computed for a unit depth of the paddles (into the page). The drag force, F_D by the current on a single paddle with unit depth is computed empirically with Eq. (5). For 2 m/s current velocity, the drag coefficient in Eq. (5) is $C_D = 1.17$, see [19], and the paddle surface area is $1 \times 0.06 = 0.6 \text{ m}^2$. The two-dimensional drag force, $F_D/l = 1404.0 \text{ N/m}$, computed by Eq. (5) is based on the incoming current velocity profile at the inlet zone. The time series of the two-dimensional hydrodynamic forces on the paddles and the empirical drag

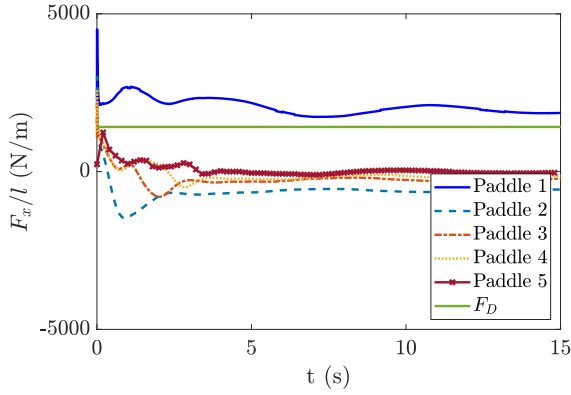


FIGURE 9. The two-dimensional horizontal forces on the paddles of the MOWT computed in this study, and the empirical drag force on a paddle, Eq. (5).

force are presented in Fig. 9. The forces computed on individual paddles are significantly different compared with the empirically calculated drag force, F_D/l , partially due the velocity profiles around the paddles are different from the incoming current velocity profile. Furthermore, paddle 1 experiences the largest horizontal force, compared with the other paddles, whereas the normalised hydrodynamic forces on paddles 3, 4 and 5 are negative, *i.e* the force on these paddles is in the opposite direction of the incoming current direction.

For $t < 4$ s, time-averaged of hydrodynamic forces on individual paddles, F_{avg} , are obtained and reported in Table 1. Comparing the time-averaged hydrodynamic forces in Table 1, paddle 1 only experiences positive horizontal force, and the averages of the hydrodynamic force on the rest of the paddles are negative. In other words, negative force on these paddles imply that for $t < 4$ s, the upstream pressure is lower than their downstream pressure. Furthermore, paddles 4 and 5 have the smallest average horizontal force in magnitude among others. Table 1 also presents the difference between the mean values of the force magnitudes on individual paddles compared with the empirical drag force, $F_{diff} = \frac{|F_{avg} - F_D|}{F_D} \times 100$. Among the five paddles of the MOWT, the forces on paddles 1 and 3 are with the lowest and the largest differences with respect to F_D/l , again partially due to different velocity profiles upstream the paddles compared with the incoming current velocity profile.

Effect of paddle spacing on the MOWT performance

As observed in Fig. 9 and Table 1, the hydrodynamic forces on paddles 2 to 5 decrease significantly to negative

TABLE 1. Averages of the two-dimensional hydrodynamic forces on the paddles, F_{avg} and the ratio of the empirical drag force, F_D , to the average forces on the paddles, F_{diff} .

Paddle No.	F_{avg} (N/m)	F_{diff}
1	1943.40	37.25 %
2	-603.47	142.62 %
3	-256.58	118.12 %
4	-180.31	112.73 %
5	-29.58	102.09 %

values compared with the hydrodynamic force on paddle 1. The design characteristics of the MOWT and the incoming velocity magnitude and profile can result in such reduction of the hydrodynamic force on the paddles in an array. In this part of the study, the effect of the spacing between the paddles on the hydrodynamic current-induced forces is investigated. For the given dimensions of the main hull in Fig. 1, various configurations are considered where the number of paddles are reduced to 4, 3 and 2 paddles. For each case, the spacing between the paddles are set such that the gap between the front of the main hull and the first paddle is kept constant at 700 mm. Next, for the MOWTs with four and three paddles, the remaining length of the bottom side of the main hull is divided by the number of paddles. Notice that to obtain the total number of paddles, one should consider the perimeter of the hull, as some paddles are above the water surface (not considered in this study). Schematic of the MOWTs with four, three and two paddles and the spacing between the paddles is shown in Fig. 10. The simulations for each modified MOWT are carried out for 15 s with the same numerical current tank and incoming current velocity profile as discussed in the previous section.

The two-dimensional hydrodynamic forces on paddles 1, 2, 3 and 4 of the MOWT with five, four, three and two paddles are computed and compared in Fig. 11. As shown in Fig. 11(a), 1st paddle of the MOWT with five paddles and the MOWT with two paddles experience the largest and the smallest hydrodynamic forces, respectively. However, in Fig. 11(b), the largest hydrodynamic force is computed on 2nd paddle of the MOWT with two paddles. Similar hydrodynamic forces are computed for 3rd and 4th paddles of the MOWTs with some oscillations at $t < 4$ s.

The total two-dimensional horizontal forces on the MOWT with two to five paddles are computed and presented in Fig. 12. The MOWT with two paddles (corre-

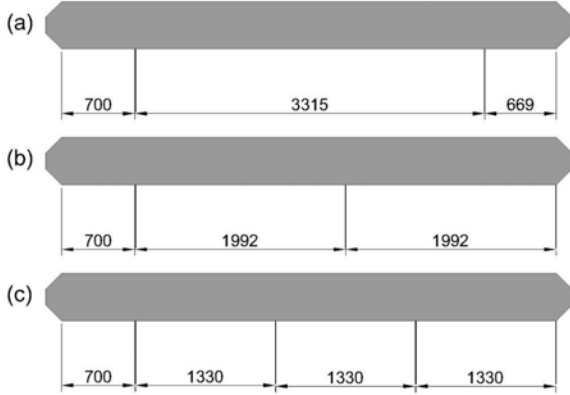


FIGURE 10. Schematic of the MOWT with (a) 2, (b) 3 and (c) 4 and the spacing between the paddles (units are in mm).

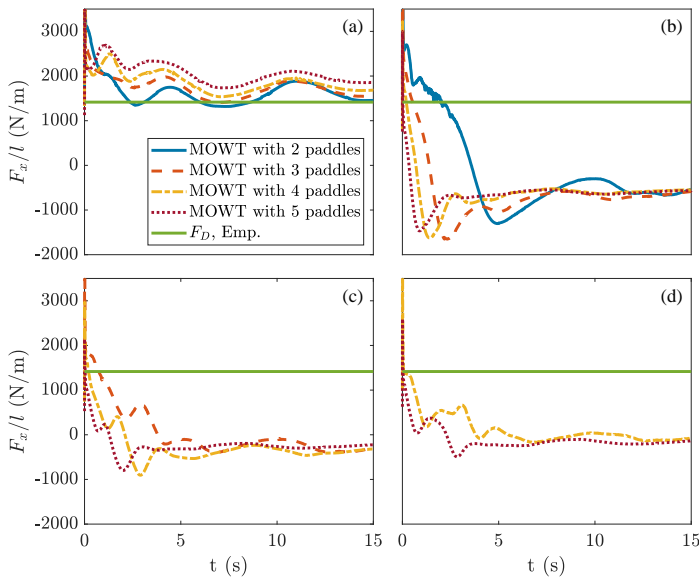


FIGURE 11. Comparison of two-dimensional horizontal forces on the (a) 1st paddle, (b) 2nd paddle, (c) 3rd paddle and (d) 4th paddle of MOWTs with 2, 3, 4 and 5 paddles and the empirically computed, drag force on a paddle.

sponding to the largest spacing between the paddles) experiences the largest total horizontal force for $t < 4$ s. This is expected as among the four configurations, the largest hydrodynamic force on the 2nd paddle is for the MOWT with two paddles. The total hydrodynamic force on the rest of the MOWTs drop sharply at approximately 2 s. However, for approximately $t > 12$ s, the total forces on the paddles for all the MOWTs converge approximately to the total horizontal force on the MOWT with five paddles.

The large spacing between the paddles of the MOWT with two paddles results in less interaction of the wake

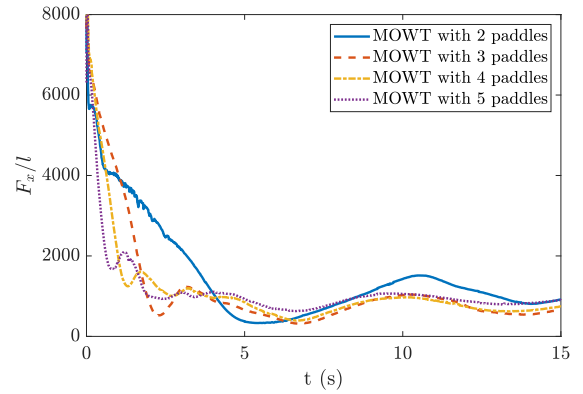


FIGURE 12. Total two-dimensional horizontal forces on the paddles of the MOWTs with 2, 3, 4 and 5 paddles.

downstream paddle 1 and the incoming flow on paddle 2. This is observed in the velocity and pressure distributions around the structure, presented in Figs. 13 and 14 for $t = 0.6$ s, 1.2 s, 3 s and 5 s. Shown in Fig. 13, both paddles experience approximately similar incoming velocity profiles and wakes at downstream. However, from approximately $t = 3$ s, the wake downstream paddle 1 changes the velocity profile around paddle 2. Finally, shown in Fig. 13 (d), the fluid velocity upstream paddle 2 is approximately zero. The reduction of the incoming flow velocity around paddle 2 explains its negative horizontal force, shown in Fig. 11(b).

The pressure distribution around paddles 1 and 2 are approximately similar at $t = 0.6$ s. At $t = 1.2$ s, the wake downstream paddle 1 grows larger and extends downstream to paddle 2. At the same time, paddle 2's wake detaches from the structure. Shown in Figs. 14(c) and (d), the wake downstream paddle 1 form a low pressure pocket within the two paddles. As mentioned earlier, the low pressure upstream of paddle 2 results in negative horizontal force.

Effect of paddle numbers on the MOWT performance

As the final parametric study, the spacing of the paddles remains constant and the number of paddles of the device are changed. Figure 15 shows the schematic of 4 modified MOWTs, with 1, 2, 3 and 4 paddles. Figure 16 shows the current-induced forces on the paddles of the MOWTs. The wake downstream the first paddle of the MOWT with 1 paddle does not interact with any other paddle on the device and thus the MOWT with 1 paddle undergoes the largest current-induced force in comparison with other modified and original MOWTs. Moreover, shown in Fig. 16, the MOWTs with 4 and 5 paddles experience the lowest horizontal forces among other.

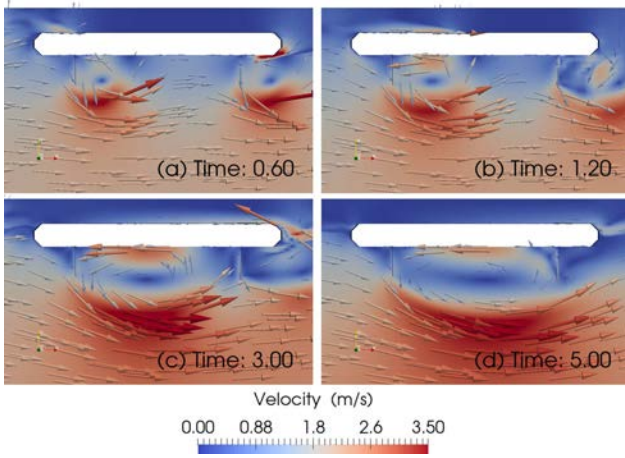


FIGURE 13. Snapshots of the velocity field at the vicinity of the MOWT with two paddles at (a) $t = 0.6$ s, (b) $t = 1.2$ s, (c) $t = 3$ s and (d) $t = 5$ s.

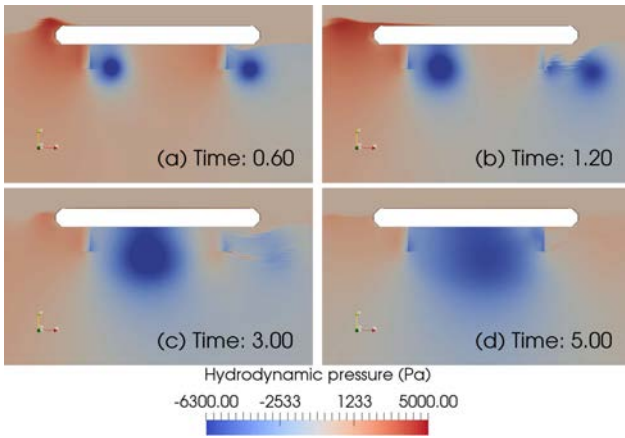


FIGURE 14. Snapshots of the pressure field at the vicinity of the MOWT with two paddles at (a) $t = 0.6$ s, (b) $t = 1.2$ s, (c) $t = 3$ s and (d) $t = 5$ s.

Conclusions

A hydrokinetic energy converter, the mass of water turbine, is introduced in this paper. The MOWT consists of several paddles connected to the main hull. The kinetic energy of the water flow results in the motion of the paddles on the main hull and this is converted to electricity by a generator. To analyse the performance of the MOWT, the fluid velocity and pressure distribution around the structure, and the hydrodynamic forces on its paddles are studied with computational fluid dynamics.

A two-dimensional numerical tank is developed and for a given uniform current velocity profile, the pressure and velocity fields at the vicinity of the structure are com-

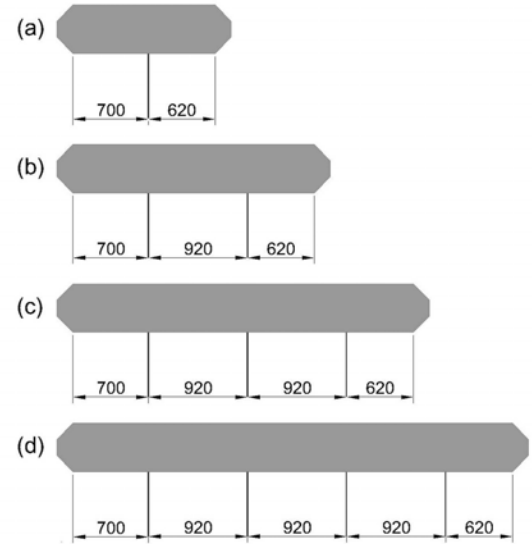


FIGURE 15. Schematic of the MOWT with (a) 1, (b) 2, (c) 3 and (d) 4 paddles with given spacings between the paddles (units are in mm).

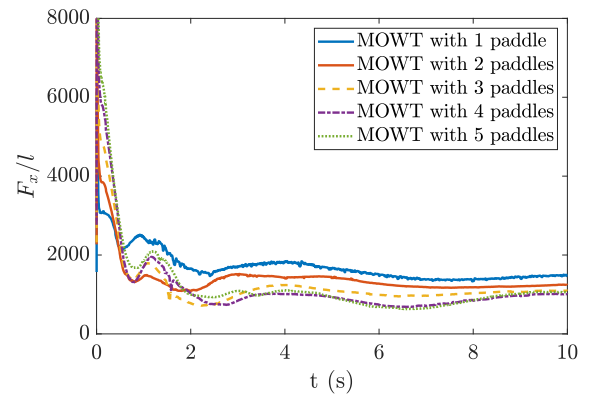


FIGURE 16. Total two-dimensional horizontal forces on the paddles of the MOWTs with 1, 2, 3, 4 and 5 paddles.

puted. The horizontal hydrodynamic forces on individual paddles are computed and compared with empirical drag force. It is shown that only the first paddle experience a positive hydrodynamic force, and approximately close to the value of the empirical drag force. However, the rest of the paddles undergo small and negative hydrodynamic forces. Parametric studies are conducted to assess the effect of the configuration of the paddles on the performance of the MOWT, namely (i) changing the spacing between the paddles where the length of the MOWT is kept constant, and (ii) changing the number of paddles where the spacing of the paddles is constant. In the former study, for three configurations, with 4, 3 and 2 paddles, the horizon-

tal hydrodynamic forces on the paddles are computed and compared. It is seen that the MOWT with 2 paddles initially undergoes larger force on its paddle 2, but in general, the total forces on the paddles are approximately the same. In the second parametric study, the effect of the number of paddles on the performance of the MOWT is examined. The MOWT with 1 paddle experiences slightly larger current-induced force compared with MOWTs with 2, 3, 4 and 5 paddles. Consequently, it is found that the number of paddles is an important design factor to optimize efficiency of the MOWT. Other factors include the hull length and the geometry of the paddles, the effect of which on the current-induced forces shall be investigated in the future.

Acknowledgements

The work of AL and MH is supported by funding from the Scottish Funding Council, and the Energy Technology Partnership of Scotland. These funding are gratefully acknowledged. Any findings and opinions contained in this paper are those of the authors and do not necessarily reflect the opinions of the funding agencies.

REFERENCES

- [1] REN21 Renewables now, 2020. Renewables 2020 global status report. Tech. rep., REN21, Paris, France.
- [2] International Hydropower Association, 2021. 2021 hydropower status report, sector trends and insights. Tech. rep., IHA, London, UK.
- [3] Yuce, M. I., and Muratoglu, A., 2015. “Hydrokinetic energy conversion systems: A technology status review”. *Renewable and Sustainable Energy Reviews*, **43**, pp. 72–82.
- [4] Lago, L. I., Ponta, F. L., and Chen, L., 2010. “Advances and trends in hydrokinetic turbine systems”. *Energy for Sustainable Development*, **14**(4), pp. 287–296.
- [5] Zainol, M. Z., Ismail, N., Zainol, I., Abu, A., and Dahalan, W., 2017. “A review on the status of tidal energy technology worldwide”. *Science International (Lahore)*, **29**(3), pp. 659–667.
- [6] Sale, D., Jonkman, J., and Musial, W., 2009. “Hydrodynamic optimization method and design code for stall-regulated hydrokinetic turbine rotors”. In ASME 28th International Conference on Ocean, Offshore, and Arctic Engineering, May 31– June 5, Honolulu, Hawaii, United States, ASME, pp. 1–17.
- [7] Zhao, R., Creech, A. C. W., Borthwick, A. G. L., Nishino, T., and Venugopal, V., 2020. “Numerical model of a vertical-axis cross-flow tidal turbine”. In Volume 9: Ocean Renewable Energy, Vol. 133, ASME, pp. 260–272.
- [8] Letcher, T. M., 2020. *Future Energy: Improved, Sustainable and Clean Options for Our Planet*, Vol. 1. Elsevier, pp. 1–792.
- [9] Ecosse-IP, 2020. Ecosse-IP, transforming sub-sea. <https://www.ecosse-ip.com/products/wave-and-tidal/>, Accessed: July 2021.
- [10] Reynolds, O., 1883. “An experimental investigation of the circumstances which determine whether the motion of water shall be direct or sinuous, and of the law of resistance in parallel channels”. *Philosophical Transactions of the Royal Society of London*, **174**(3), dec, pp. 935–982.
- [11] Ferziger, J. H., and Peric, M., 2012. *Computational methods for fluid dynamics*, Vol. 3. Springer Science & Business Media, pp. 1–596.
- [12] Greenshields, C. J. G., 2018. Openfoam, user guide. Tech. Rep. version 6, July, 2011-2018 OpenFOAM Foundation Ltd.
- [13] Jacobsen, N. G., 2017. Waves2foam manual. Tech. Rep. August, Deltares.
- [14] Ren, B., He, M., Dong, P., and Wen, H., 2015. “Nonlinear simulations of wave-induced motions of a freely floating body using wcsph method”. *Applied Ocean Research*, **50**, pp. 1–12.
- [15] Li, S., Hayatdavoodi, M., and Ertekin, R. C., 2020. “On wave-induced elastic deformations of a submerged wave energy device”. *Journal of Marine Science and Application*, **19**(3), pp. 317–338.
- [16] Kostikov, V., Hayatdavoodi, M., and Ertekin, R. C., 2021. “Hydroelastic interaction of nonlinear waves with floating sheets”. *Theoretical Computational Fluid Dynamics*, **35**(4), pp. 515–537.
- [17] Kostikov, V., Hayatdavoodi, M., and Ertekin, R. C., 2021. “Drift of elastic floating ice sheets by waves and current, part i: single sheet”. *Proceedings of the Royal Society A*, **477**(2254), p. 20210449.
- [18] Venugopal, V., Varyani, K. S., and Westlake, P. C., 2009. “Drag and inertia coefficients for horizontally submerged rectangular cylinders in waves and currents”. *Proceedings of the Institution of Mechanical Engineers Part M: Journal of Engineering for the Maritime Environment*, **223**(1), pp. 121–136.
- [19] Hoerner, S. F., 1958. *Fluid-dynamic drag : practical information on aerodynamic drag and hydrodynamic resistance*, 2nd ed. Published by the author, pp. 1–460, Bakersfield, CA, USA.